

Dynamic colloidal assembly pathways via low dimensional models

Yuguang Yang, Raghuram Thyagarajan, David M. Ford, and Michael A. Bevan

Citation: [The Journal of Chemical Physics](#) **144**, 204904 (2016); doi: 10.1063/1.4951698

View online: <https://doi.org/10.1063/1.4951698>

View Table of Contents: <http://aip.scitation.org/toc/jcp/144/20>

Published by the [American Institute of Physics](#)

Articles you may be interested in

[Colloidal cluster crystallization dynamics](#)

The Journal of Chemical Physics **137**, 134901 (2012); 10.1063/1.4754870

[A Smoluchowski model of crystallization dynamics of small colloidal clusters](#)

The Journal of Chemical Physics **135**, 154506 (2011); 10.1063/1.3652967

[Interfacial colloidal rod dynamics: Coefficients, simulations, and analysis](#)

The Journal of Chemical Physics **147**, 054902 (2017); 10.1063/1.4995949

[Effective colloidal interactions in rotating magnetic fields](#)

The Journal of Chemical Physics **147**, 074903 (2017); 10.1063/1.4986501

[Interfacial colloidal sedimentation equilibrium. I. Intensity based confocal microscopy](#)

The Journal of Chemical Physics **127**, 164708 (2007); 10.1063/1.2794340

[Interactions and microstructures in electric field mediated colloidal assembly](#)

The Journal of Chemical Physics **131**, 134704 (2009); 10.1063/1.3241081

PHYSICS TODAY

WHITEPAPERS

ADVANCED LIGHT CURE ADHESIVES

READ NOW

Take a closer look at what these
environmentally friendly adhesive
systems can do

PRESENTED BY



Dynamic colloidal assembly pathways via low dimensional models

Yuguang Yang,¹ Raghuram Thyagarajan,² David M. Ford,² and Michael A. Bevan^{1,a)}

¹Chemical and Biomolecular Engineering, Johns Hopkins University, Baltimore, Maryland 21218, USA

²Chemical Engineering, University of Massachusetts, Amherst, Massachusetts 01003, USA

(Received 3 February 2016; accepted 10 May 2016; published online 31 May 2016)

Here we construct a low-dimensional Smoluchowski model for electric field mediated colloidal crystallization using Brownian dynamic simulations, which were previously matched to experiments. Diffusion mapping is used to infer dimensionality and confirm the use of two order parameters, one for degree of condensation and one for global crystallinity. Free energy and diffusivity landscapes are obtained as the coefficients of a low-dimensional Smoluchowski equation to capture the thermodynamics and kinetics of microstructure evolution. The resulting low-dimensional model quantitatively captures the dynamics of different assembly pathways between fluid, polycrystal, and single crystals states, in agreement with the full N -dimensional data as characterized by first passage time distributions. Numerical solution of the low-dimensional Smoluchowski equation reveals statistical properties of the dynamic evolution of states vs. applied field amplitude and system size. The low-dimensional Smoluchowski equation and associated landscapes calculated here can serve as models for predictive control of electric field mediated assembly of colloidal ensembles into two-dimensional crystalline objects. Published by AIP Publishing. [<http://dx.doi.org/10.1063/1.4951698>]

INTRODUCTION

Self-assembly refers to dynamical processes where predefined components spontaneously organize into ordered structures. Self-assembly is considered as a key bottom-up approach to fabricate novel micro- and nano-scale materials.^{1–3} Modeling studies of self-assembly generally focus on predicting the resulting equilibrium or steady-state structures as a function of particle interactions, particle shapes, temperature, and concentration.^{4,5} Such equilibrium information is important for yielding design rules for building blocks capable of assembling into complex structures. However, the existence of metastable states, kinetic bottlenecks, and competing pathways during dynamical assembly processes can prevent self-assembling systems from reaching thermodynamically stable states on experimentally accessible time scales.^{6,7}

In addition to understanding the thermodynamics of self-assembly, it is beneficial to uncover the underlying driving forces and dynamics governing self-assembly processes. In general, dynamic models should contain information about the existence of metastable states as well as the expected times for transitions between states. Ideally, construction of such dynamic models at different thermodynamic conditions can enable the rational design of optimal kinetic pathways to achieve desired states by performing state-dependent temporal actuation of the system.^{8–10} The evolution of stochastic dynamical self-assembling systems can be formulated using, for example, a master equation,¹¹ Fokker Planck equation,¹² or Smoluchowski equation (SE).¹³

The Smoluchowski equation (SE) is suitable to describe Markovian stochastic processes for thermally equilibrated systems. The SE contains thermodynamic and kinetic information in its coefficients and has been applied to complex systems involving protein folding,¹⁴ colloidal assembly,¹⁵ and micellization.¹³ In such complex systems, the SE is usually not parameterized by $3N$ particle coordinates, but instead by low-dimensional coordinates capturing the collective behavior of the system. The procedure to obtain a suitable SE can be briefly described as follows: (1) identifying the dimensionality of the dynamics (*i.e.*, number of slow modes of collective motion) via trajectory analysis (*e.g.*, principal component analysis,¹⁶ diffusion mapping^{17,18}), (2) finding a suitable set of coordinates, which are often scalar functions of the $3N$ particle coordinates, to capture the slow modes (usually heuristically chosen based on coarse grained physics), and (3) obtaining coefficients for the SE in the low dimensional coordinates via fitting schemes (*e.g.*, local linear fitting,¹⁹ global Bayesian inference²⁰). The SE coefficients include the free energy landscape, W , which reflects free energy differences between different configurations, and the diffusivity landscape (DL), D , which captures the mobility of trajectories in configuration space. The SE solution describes the probability distribution of states as a function of time, thus providing a dynamic statistical model for assembly processes. We have previously applied these tools to develop dynamic models of depletion attraction mediated colloidal cluster crystallization,^{15,20} which we applied in subsequent studies focused on optimal control of such systems.^{9,10}

In this work, we present a systematic framework for building a low-dimensional model to capture the assembly of finite sized quasi-2D colloidal crystals using Brownian Dynamic (BD) simulations matched to our previous experiments.²¹ The experiment involves using an electric field

^{a)}Author to whom correspondence should be addressed. Electronic mail: mabevan@jhu.edu

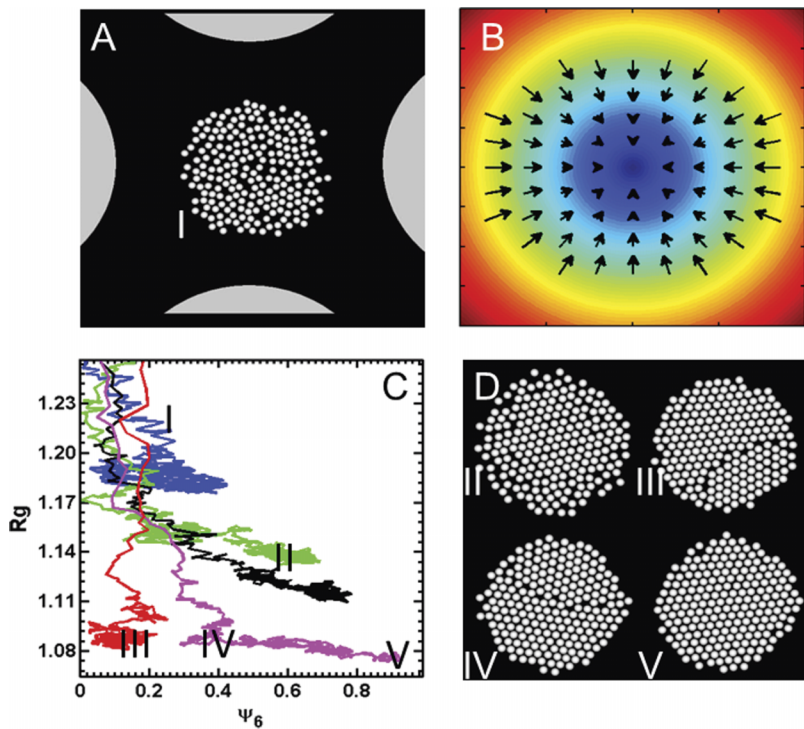


FIG. 1. (a) Top view of simulated experiment of quasi-2D configuration of $N = 210$ colloidal particles ($2a = 3 \mu\text{m}$) compressed within a quadrupolar electrode (with electrode gap of $d_g = 100 \mu\text{m}$). (b) Electric field magnitude contour plot within quadrupole electrode center (Eq. (5)) with arrows indicating relative magnitude and direction of force due to dipole-field interactions (Eqs. (2) and (7)) that concentrates particles in quadrupole center. (c) Typical colloidal assembly trajectories in the order parameter pair (ψ_6, R_g) for a system size of $N = 210$ at voltages of (see definition of nondimensional V^* in Eq. (21)) where $V^* = 1$ corresponds to thermodynamic condition for perfect crystal as free energy minimum configuration²¹: $V^* = 0.42$ (blue), $V^* = 0.5$ (green), $V^* = 0.57$ (black), $V^* = 0.80$ (pink), and $V^* = 0.80$ (red). Representative states in part (c) are marked as (rendered in part (d) with exceptions noted): I (initial fluid state, part (a)), II (crystal configuration coexisting with peripheral fluid particles), III (low order bicrystal), IV (higher order bicrystal), and V (single crystal with a few particles still experiencing thermal motion at crystal periphery).

to compress colloids in the center of a quadrupole (Fig. 1). This simple assembly problem demonstrates the basic features of competing pathways, metastable states, and relaxation from metastable state, and we have quantified the interaction potentials,^{22–24} system size dependent thermodynamics and kinetics,²¹ and grain boundary formation.⁷ As such, it serves as a well characterized and understood test case for a general low-dimensional modeling method. From an application standpoint, it is interesting in its own right for reconfigurable colloidal materials and devices,^{25,26} which we have demonstrated in circuit elements,²⁷ feedback controlled colloidal crystal assembly,^{8,28} and in the formation of three dimensional crystals.²⁹ Assembly trajectories in candidate order parameters (Fig. 1(c)) help to show the general approach investigated in this work, where parameters that quantify condensation and order together capture the relevant states and dynamics as particles move from fluid to polycrystal to single crystal states (Fig. 1(d)). Our results demonstrate the ability to fit a low-dimensional SE to a large number of BD simulations to obtain the W and D coefficients, which we relate to physical states and dynamic processes associated with colloidal crystal assembly vs. applied field amplitude and system size (number of particles). Our modeling efforts in this work include dimensionality reduction, order parameter estimation, model validation, and physical interpretation of the dynamic model.

THEORY

Interaction potentials

In this paper, we model electric field mediated quasi-2D colloidal assembly in a quadrupole electrode using previously measured potentials.^{22–24} In brief, colloidal particles interact

via electrostatic double layer repulsion, dipole-field potentials, and dipole-dipole potentials. The electrostatic repulsion between particle i and j is given as³⁰

$$u_{e,i,j}^{pp}(r_{ij}) = B^{pp} \exp[-\kappa(r_{ij} - 2a)], \quad (1)$$

where r_{ij} is center-to-center distance between particles, a is particle radius, and B^{pp} is the pre-factor for pair electrostatic repulsion between colloidal particles.³⁰ The dipole-field potential for particle i in a spatially varying electric field is given as²³

$$u_{de,i}^{pf}(\mathbf{r}) = -2kT\lambda f_{cm}^{-1}[E(\mathbf{r}_i)/E_0]^2, \\ \lambda = \frac{\pi\epsilon_m a^3 (f_{cm} E_0)^2}{kT}, \quad (2)$$

where \mathbf{r}_i is the position of particle i , k is Boltzmann's constant, T is temperature, f_{cm} is the Clausius-Mossotti factor, λ is a non-dimensional amplitude, ϵ_m is the medium dielectric constant, $E(\mathbf{r}_i)$ is the local electric field peak magnitude at the particle position, and E_0 is given by

$$E_0 = 8^{-0.5} (V_{pp}/d_g), \quad (3)$$

where V_{pp} is the peak-to-peak voltage and d_g is the electrode gap. The dipole-dipole interaction potential between particles i and j is given by²⁴

$$u_{dd,i,j}^{pp}(\mathbf{r}_{ij}) = -kT\lambda P_2(\cos\theta_{ij})(2a/r_{ij})^3[E(\mathbf{r}_i)/E_0]^2, \quad (4)$$

where $P_2(\cos\theta_{ij})$ is the second Legendre polynomial and θ_{ij} is the angle between the line connecting particle centers and the electric field line direction. The electric field in the quadrupole center is approximated as^{8,28,29}

$$\left| \frac{E(\mathbf{r}_i)}{E_0} \right| = \frac{4r}{d_g}, \quad (5)$$

where $r = (x^2 + y^2)^{0.5}$, and x and y are Cartesian coordinates with origin at the quadrupole center.

Colloidal particle dynamics

Particle dynamics in quasi-2D configurations near a planar surface are modelled using previously reported methods³¹ with several modifications. The equation of motion for Brownian particles is given as³²

$$\mathbf{r}(t + \Delta t) = \mathbf{r}(t) + \frac{\mathbf{D}^P}{kT}(\mathbf{F}^P + \mathbf{F}^B)\Delta t + \nabla \cdot \mathbf{D}^P \Delta t, \quad (6)$$

$$\langle \mathbf{F}^B \rangle = 0, \quad \langle \mathbf{F}^B(t_1)(\mathbf{F}^B(t_2))^T \rangle = 2(kT)^2(\mathbf{D}^P)^{-1}\delta(t_1 - t_2),$$

where \mathbf{r} is the $2N$ dimensional position vector, \mathbf{F}^B is the Brownian force vector, and \mathbf{F}^P is the total conservative force vector and the superscript T denotes transpose. The components of \mathbf{F}^P describing the conservative force acting on particle i are given as

$$\mathbf{F}_i^P = -\nabla_{\mathbf{r}_i} \left[u_{de,i}^{pf} + \sum_{j \neq i} (u_{e,i,j}^{pp} + u_{dd,i,j}^{pp}) \right] \quad (7)$$

and \mathbf{D}^P is the diffusivity tensor, related to grand resistance tensor \mathbf{R}^P via Stokes-Einstein relation $\mathbf{D}^P = kT(\mathbf{R}^P)^{-1}$, where \mathbf{R}^P is given by³³

$$\mathbf{R}^P = (\mathbf{M}^\infty)^{-1} + \mathbf{R}_{2B} - \mathbf{R}_{2B}^\infty, \quad (8)$$

which includes pair-wise lubrication interactions, \mathbf{R}_{2B} , and many-bodied far-field interactions, $(\mathbf{M}^\infty)^{-1} - \mathbf{R}_{2B}^\infty$, above a no-slip plane.^{34,35}

Diffusion mapping

From a set of particle configurations (*i.e.*, snapshots), we compute a Markov probability matrix, \mathbf{M} , whose elements M_{ij} are a measure of the probability of hopping between the snapshots i and j . We denote each snapshot as a set X composed of the coordinate vectors of all particles (*i.e.*, $X = (\mathbf{r}_1, \mathbf{r}_2, \dots, \mathbf{r}_N)$). To construct \mathbf{M} , a measure of the distance between snapshots is required that resides in a $2N$ dimensional space. First, it is necessary to calculate a distance matrix, Δ , whose elements Δ_{ij} are the distance metric between two snapshots X_i and X_j . In this work, the distance metric is a weighted combination of the Hausdorff distance matrix, \mathbf{H} ,²⁰ and a local orientation distance matrix, \mathbf{O} , given as

$$\begin{aligned} \Delta_{ij} &= \left[(\mathbf{H}_{ij}/\|\mathbf{H}\|_F)^2 + (\mathbf{O}_{ij}/\|\mathbf{O}\|_F)^2 \right]^{0.5}, \\ \mathbf{H}_{ij} &= \max_{\mathbf{r}_m \in X_i} \min_{\mathbf{r}_n \in X_j} \|\mathbf{r}_m - \mathbf{r}_n\|_2, \\ \mathbf{O}_{ij} &= \min_{\theta_t} \|h_i(\theta) - h_j(\theta + \theta_t)\|_2, \end{aligned} \quad (9)$$

where $\|\cdot\|_F$ denotes the Frobenius norm, and $h_i(\theta)$ is the normalized bonding angle histogram for snapshot i , where θ_t is the offset in order to achieve the global optimal alignment. The geometric average of \mathbf{H} and \mathbf{O} is motivated by considering the norm of a two-component vector. Hausdorff distance is the greatest of all distances from a particle in one snapshot to the closest particle in another snapshot and has been used previously in systems of unlabeled particles.^{18,20} The bonding angle is the angle of the vector $(\mathbf{r}_i - \mathbf{r}_j)$ joining neighboring particles i, j with respect to the x-axis. We then

define the kernel matrix using $\mathbf{K}_{ij} = \exp(-\Delta_{ij}^2/2\varepsilon^2)$, with ε being the parameter that sets the correlation length in the system. The parameter ε is chosen using a technique outlined elsewhere.^{36,37} Each row of the kernel matrix \mathbf{K} is normalized to obtain \mathbf{M} as

$$\mathbf{M}_{ij} = \frac{\mathbf{K}_{ij}}{\sum_j \mathbf{K}_{ij}}, \quad (10)$$

where the solution of the right eigenvalue problem,

$$\mathbf{M}\mathbf{v} = \lambda \mathbf{v}, \quad (11)$$

produces an eigenvalue spectrum, λ_n , and corresponding set of eigenvectors, \mathbf{v} . The eigenvalue spectrum provides insight into the number of dimensions required to describe the process dynamics. The corresponding eigenvectors provide a low dimensional embedding of the $2N$ dimensional configurations in the data set. In this work, the eigenvectors are not used directly as order parameters but are correlated against candidate coarse variables to identify a suitable set of order parameters.

Order parameters

Following procedures similar to our previous study,²⁰ here we define two order parameters, R_g and ψ_6 , as order parameters ultimately to be employed in a low-dimensional dynamic model (in the section titled “Results and Discussion,” we provide justification for their use based on diffusion mapping). The degree of condensation of colloidal particles is captured using the radius of gyration, R_g , which is given as

$$R_g = 0.5N^{-1} \left[\sum \|\mathbf{r}_i - \mathbf{r}_j\|_2^2 \right]^{0.5} / R_{g,HEX} \quad (12)$$

which is a measure of the root mean square distance between particles within an ensemble normalized by a factor $R_{g,HEX}$. This factor is the radius of gyration for 2D HCP (hexagonal closed packing) particles within regular polygon morphologies given by⁸

$$R_{g,HEX} = 5^{0.5} 3^{-1} a N^{0.5}, \quad (13)$$

where a is the particle radius and N is the particle number in the system. The degree of global orientational order in particle configurations was obtained from particle coordinates using³⁸

$$\psi_{6,j} = \frac{1}{N_{C,j}} \sum_{k=1}^{N_{C,j}} e^{i6\theta_{jk}}, \quad (14)$$

$$\psi_6 = \frac{1}{N} \left| \sum_j^N \psi_{6,j} \right|, \quad (15)$$

where $\psi_{6,j}$ is the local six-fold bond orientation order parameter of particle j , $N_{C,j}$ is the number of neighbors within the first $g(r)$ peak (coordination radius) of particle j , θ_{jk} is the angle between particle j and each neighboring particle with an arbitrary reference direction, and ψ_6 is the global bond orientation order determined by averaging over all particles, which produces values between 0 for disordered fluids and perfect bicrystals (*i.e.*, crystal with equal sized domains misoriented by 30°) and 1 for defect-free, single domain hexagonal packed lattices.

Low-dimensional Smoluchowski and Langevin equations

Colloidal assembly trajectories are modeled using a low-dimensional Smoluchowski Equation (SE) parameterized by order parameter coordinates given as^{7,15,20}

$$\frac{\partial p(\mathbf{x}, t)}{\partial t} = \nabla \cdot \mathbf{D}(\mathbf{x}) \cdot [(kT)^{-1} \nabla W(\mathbf{x}) + \nabla] p(\mathbf{x}, t), \quad (16)$$

where $p(\mathbf{x}, t | \mathbf{x}_0, 0)$ is the probability density for system to be at a state characterized by the coordinate $\mathbf{x} = (\psi_6, R_g)$ at time t given that the system starts at \mathbf{x}_0 at $t = 0$. The coefficient, $\mathbf{D}(\mathbf{x})$, which is a symmetric tensor, is the diffusivity landscape (DL) consisting of two diagonal terms $D_{\psi_6\psi_6}$, $D_{R_gR_g}$, and two off-diagonal terms $D_{\psi_6R_g}$ and $D_{R_g\psi_6}$. The coefficient $W(\mathbf{x})$ is the free energy landscape (W), which captures the free energy of every configuration based on its coordinate $\mathbf{x} = (\psi_6, R_g)$. The SE describes the probability density evolution in the order parameter space, given the initial probability distribution. The evolution is determined by the right hand side propagator, which contains $\mathbf{D}(\mathbf{x})$ and $W(\mathbf{x})$ that dictate the kinetic and thermodynamic aspects of the system. Our assumption implies that the stationary distribution from Eq. (16) is the thermodynamic equilibrium probability distribution $p(\mathbf{x}) = \exp[-W(\mathbf{x})/kT]$, which can be obtained by setting the right-hand-side to be zero.

The coefficients $\mathbf{D}(\mathbf{x})$ and $W(\mathbf{x})$ in Eq. (16) can be extracted from assembly trajectories using a linear fitting procedure.^{7,15,20} In brief, the initial slope of the mean displacement vs. time and mean displacement variance vs. time (*i.e.*, mean squared displacement, covariance matrix) at each local coordinate can be used to evaluate drift, $\mathbf{v}(\mathbf{x})$, and diffusivity tensor, $\mathbf{D}(\mathbf{x})$, as

$$\begin{aligned} \mathbf{v}_i(\mathbf{x}) &= \frac{\partial \mu_i}{\partial \Delta t} = \lim_{\Delta t \rightarrow 0} \frac{1}{\Delta t} \langle (\chi(t + \Delta t) - \chi(t))_i \rangle_{\chi(t)=\mathbf{x}}, \\ \mathbf{D}_{ij}(\mathbf{x}) &= \frac{1}{2} \frac{\partial \sigma_{ij}^2}{\partial \Delta t} \\ &= \lim_{\Delta t \rightarrow 0} \frac{1}{2\Delta t} \langle (\chi(t + \Delta t) - \chi(t))_i (\chi(t + \Delta t) - \chi(t))_j \rangle_{\chi(t)=\mathbf{x}}, \end{aligned} \quad (17)$$

where χ is the instantaneous order parameter coordinate \mathbf{x} , and the bracket indicates the average of all trajectories sampling each coordinate. The free energy landscape, $W(\mathbf{x})$, is related to the drift as (by expanding the derivative of Eq. (16) and comparing with the Fokker-Planck equation¹²)

$$-\frac{\mathbf{D}}{kT} \cdot \nabla W + \nabla \cdot \mathbf{D} = \mathbf{v}, \quad (18)$$

where the first term on the left has the typical form of mobility coefficient multiplied by the gradient of the energy, and the second term is the noise-induced drift.^{12,39} This expression can be integrated to obtain

$$W(\mathbf{x}_2) - W(\mathbf{x}_1) = -kT \int_{\mathbf{x}_1}^{\mathbf{x}_2} (\mathbf{D})^{-1} \cdot (\mathbf{v} - \nabla \cdot \mathbf{D}). \quad (19)$$

The coefficients $\mathbf{D}(\mathbf{x})$ and $W(\mathbf{x})$ can also be used to produce a low dimensional Langevin dynamic (LDLD) equation given by

$$\mathbf{x}(t + \Delta t) = \mathbf{x}(t) - \frac{\mathbf{D}}{kT} \cdot \nabla W \Delta t + \nabla \cdot \mathbf{D} \Delta t + \sqrt{2\mathbf{D}\Delta t} \cdot \zeta, \quad (20)$$

where ζ is a vector of Gaussian random numbers with zero mean and unity variance based on the Ito convention.⁴⁰ The LDLD equation can be used to directly generate trajectories in the low-dimensional order parameter space.

METHODS

Brownian and Langevin dynamic simulations

Particle scale dynamics were simulated in the canonical ensemble using Brownian Dynamics (BD) via Eq. (6). In particular, ~2000-4000 BD simulations were performed for different system sizes ($N = 110, 210, 300$), different applied electric fields, and from many different initial configurations spanning dilute fluid to crystalline states. The initial configurations used to launch simulations were chosen adaptively to ensure that every point in the order parameter space has ~200 samplings to reduce variance in subsequent analyses. This single large set of BD simulations was used for extracting SE coefficients (Figs. 3, 4, and 7) and first passage time characterization (Fig. 5). Simulation parameters are reported in Table I. The electric field in each simulation is computed via Eq. (3) using voltages normalized as

$$V^* = V_{pp}/V_{xtal}, \quad (21)$$

$$\begin{aligned} V_{xtal} &= a_0 N^{-b_0}, \\ a_0 &= 7.15 + 4.10 \cdot 10^{-3} \kappa^{-1}, \\ b_0 &= 0.219 + 4.24 \cdot 10^{-4} \kappa^{-1}, \end{aligned} \quad (22)$$

where V_{pp} is the peak-to-peak applied voltage, and V_{xtal} is the lowest voltage to crystallize all particles based on system size and Debye length, κ^{-1} , as reported in our previous work.²¹ For each simulation, a 0.1 ms integration time step was used for at least 1.5×10^7 steps (so that each simulation reaches equilibrium). Particle coordinates were stored every 125 ms for calculation of ψ_6 and R_g . Particles in BD simulations were fixed within a 2D plane. To reduce computational cost in the BD simulations, hydrodynamic interactions were approximated by the diagonal elements of \mathbf{D}^P computed using Eq. (8), which were parameterized in a look-up table vs. the configuration R_g and the distance of particle i to the configuration center of mass (see previous work for details⁷). Low Dimensional Langevin Dynamics (LDLD) for the first passage time characterization (Fig. 5) were simulated via the equation of motion in Eq. (20) using the $W(\mathbf{x})$ and $\mathbf{D}(\mathbf{x})$ obtained from Eqs. (17) and (19) using an integration time step of $\Delta t = 0.125$ s.

Diffusion mapping

For the diffusion mapping analysis, a large number of configurations (snapshots) were generated using BD simulations for a system size of $N = 210$ with $V^* = 0.80$. The data set contained ~8000 configurations covering all of configuration space including fluid, polycrystalline, and crystalline states. Each configuration snapshot in the data set was processed to remove the translational degrees of freedom by setting the configuration origin as the center-of-mass as

TABLE I. Parameters for simulations of colloidal particles in a quadrupole electrode.

Variable	Value
N^a	110, 210, 300
a (nm) ^b	1400
κ^{-1} (nm) ^c	10
B^{PP} (kT) ^d	3206
f_{cm}^e	-0.4667
ϵ_m/ϵ_0^f	78
d_g (μm) ^g	100
T ($^\circ\text{C}$) ^h	20
R_g, HEX (nm) ⁱ	15 122 ($N = 210$); 10 944 ($N = 110$); 18 074 ($N = 300$)
V_{xtal} (V) ^j	1.89 ($N = 210$); 2.71 ($N = 110$); 1.43 ($N = 300$)
V (V) ^k	0.8, 0.94, 1.07, 1.51 ($N = 210$); 2.3 ($N = 110$); 1.07 ($N = 300$)
V^* (V) ^l	(0.42, 0.5, 0.57, 0.80) ($N = 210$); 0.85 ($N = 110$); 0.75 ($N = 300$)
λ^m	2.5, 3.5, 4.5, 9 ($N = 210$); 21 ($N = 110$); 4.5 ($N = 300$)

^aNumber of particles.^bParticle size.^cDebye screening length.^dElectrostatic potential pre-factor.^eClausius-Mossotti factor for 1 MHz AC field.^fMedium permittivity.^gElectrode spacing.^hTemperature.ⁱRadius of gyration for 2D HCP particles within regular hexagon morphologies.^jLowest voltage to crystallize system.^kApplied voltage.^lNormalized voltage.^mNon-dimensional field strength.

$$\mathbf{r}'_i = \mathbf{r}_i - \bar{\mathbf{r}}, \quad \bar{\mathbf{r}} = \frac{1}{N} \sum_{i=1}^N \mathbf{r}_i, \quad i = 1, 2, \dots, N, \quad (23)$$

where the translated coordinates form a data matrix, $X = [\mathbf{r}'_1, \mathbf{r}'_2, \dots, \mathbf{r}'_N]$, which can be used to find the eigenvector \mathbf{n}_1 of matrix with the largest magnitude XX^T as principle angle with the x-axis as $\theta = \cos^{-1}(\mathbf{n}_1 \cdot \mathbf{e}_1)$. This angle is used to remove rotational degrees of freedom using a rotational transformation given as

$$\mathbf{r}''_i = \begin{pmatrix} \cos(\theta) & \sin(\theta) \\ -\sin(\theta) & \cos(\theta) \end{pmatrix} \mathbf{r}'_i, \quad (24)$$

where the position vectors \mathbf{r}'' is used as the input to the diffusion mapping analysis, so as to not include dynamics in these additional degrees of freedom, but instead

capture microstructural dynamic processes. The bonding angle histogram is discretized into 128 bins from $-\pi$ to π .

Smoluchowski equation solution

The coefficients $\mathbf{D}(\mathbf{x})$ and $W(\mathbf{x})$ in Eq. (16) can be extracted from assembly trajectories using the linear fitting procedure^{7,15,20} described in Eqs. (17)-(19). In this work, R_g and ψ_6 coordinates are discretized with a resolution of 0.0032 and 0.025. After the coefficients are obtained, the resulting SE (Eq. (16)) can be numerically solved to obtain the probability evolution $p(\mathbf{x}, \Delta t | \mathbf{x}_0, 0)$ at different observation times, Δt , for given initial conditions. In this work, the SE is solved using explicit upwind differentiation for parabolic partial differential equations with zero-flux boundary conditions.⁴¹ The discrete version of Eq. (16) is given as

$$p_{i,j}^{n+1} - p_{i,j}^n \approx \frac{D_{i+1,j}^{\psi_6} p_{i+1,j}^n - 2D_{i,j}^{\psi_6} p_{i,j}^n + D_{i-1,j}^{\psi_6} p_{i-1,j}^n}{(\Delta \psi_6)^2} \Delta t + \frac{D_{i,j+1}^{R_g} p_{i,j+1}^n - 2D_{i,j+1}^{R_g} p_{i,j+1}^n + D_{i,j-1}^{R_g} p_{i,j-1}^n}{(\Delta R_g)^2} \Delta t + \frac{\max(v_{i-1,j}^{\psi_6} p_{i-1,j}^n, 0) + \min(v_{i+1,j}^{\psi_6} p_{i+1,j}^n, 0) - v_{i,j}^{\psi_6} p_{i,j}^n}{\Delta \psi_6} \Delta t + \frac{\max(v_{i,j-1}^{R_g} p_{i,j-1}^n, 0) + \min(v_{i,j+1}^{R_g} p_{i,j+1}^n, 0) - v_{i,j}^{R_g} p_{i,j}^n}{\Delta R_g} \Delta t, \quad (25)$$

where the subscripts indicate order parameter grid points, the superscript, n , on p denotes the time step, the superscript order parameter on v denotes the drift component from Eq. (17), and

the superscripts in D denotes the diagonal components in \mathbf{D} from Eq. (17). The off-diagonal components of \mathbf{D} are ignored in this work for simplicity and because they are relatively

small compared to the diagonal terms. One constraint on the set of equations given by Eq. (25) is that the sum of the right-hand-side of all equations must be zero via the conservation of probability. Eq. (25) is discretized with a resolution of $\Delta\psi_6 = 0.032$, $\Delta R_g = 0.0025$, and $\Delta t = 0.01$ s.

First passage time distributions (FPTDs)

To verify the extracted coefficients in Eq. (17), we compare BD (Eq. (6)) and LDLD (Eq. (20)) simulations based on first passage time distributions between different states. These different states are chosen to capture the condensation process (fluid to polycrystal), grain boundary migration process (polycrystal to single domain crystal), as well as the combination of the two (fluid to single domain crystal). The first passage time distributions are constructed by counting the first arrival time to specified ending states of trajectories starting from the same initial state. The same BD trajectory data used to obtain the SE coefficients were used to construct first passage time distributions. For LDLD simulation results, statistics were first collected from 4000 trajectories initiated in fluid and polycrystalline states (from 40 grid points with 100 different random number generator seeds). After initial sampling, another 4000 simulations were performed for states with insufficient sampling. These 8000 dynamic trajectories in low dimensional space via LDLD

were used to construct first passage time distributions between different states.

RESULTS AND DISCUSSION

Dimensionality from diffusion mapping

The first step towards building a low dimensional Smoluchowski model is to identify the number and the appropriate choice of order parameters. To this end, we have used a machine learning technique, called diffusion mapping, which identifies the intrinsic manifold of a large data set and provides a suitable low dimensional representation.¹⁸ We have applied the diffusion maps technique to smaller systems in our earlier work to build low dimensional models.²⁰ In the current implementation of diffusion mapping, we use a new composite distance metric (Δ) based in complementary metrics for both condensation (**H**) and ordering (**O**) processes important to colloidal crystallization. We apply the analysis to simulation data that were previously matched to experiments, which enables high spatial and temporal resolution and statistical sampling to avoid some issues^{42,43} when working directly with experimental microscopy data (which can be overcome when treated carefully⁴⁴).

Fig. 2 shows results of a diffusion mapping⁴⁵ analysis of a large number of Brownian Dynamic (BD) simulations

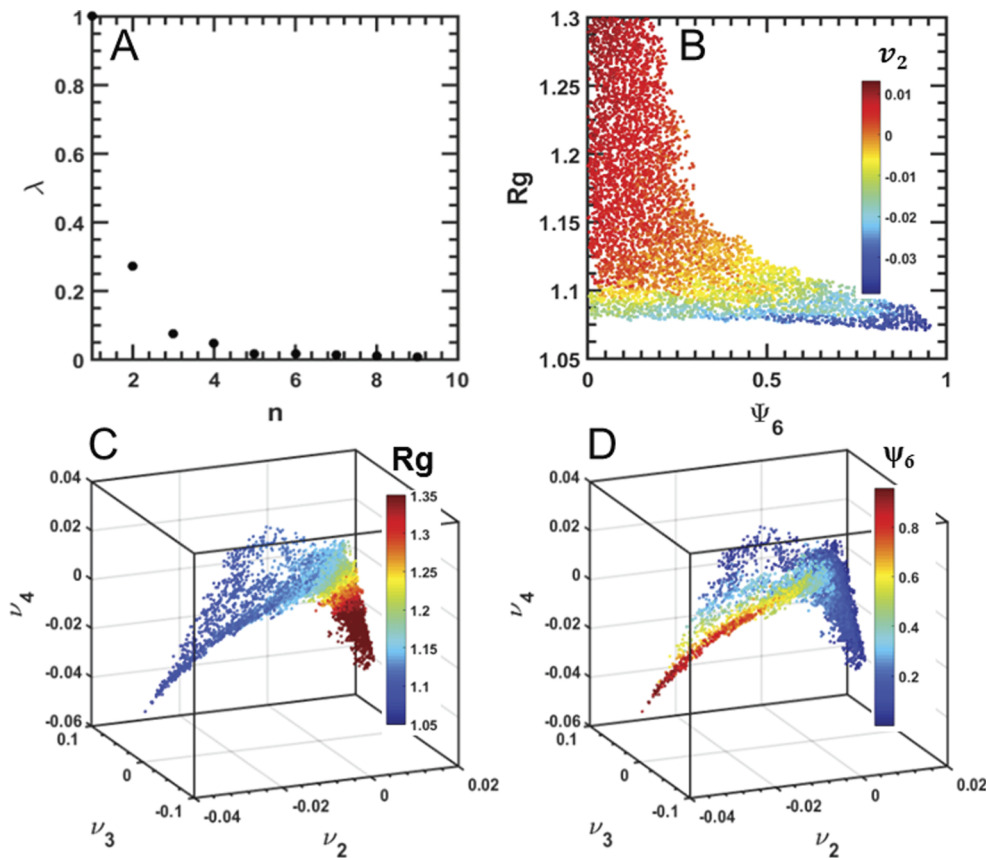


FIG. 2. (a) Eigenvalue spectrum obtained from diffusion mapping (Eqs. (9)-(11)) the process of electric field mediated colloidal assembly in a quadrupole electrode (see Fig. 1) for a system size of $N = 210$ and a non-dimensional applied voltage of $V^* = 0.8$. (b) Plot of ~8000 configurations sampled in BD simulations plotted in (Ψ_6, R_g) space and colored by values of first non-trivial eigenvector, v_2 , shows good sampling of final order parameters. Bottom two plots show points indicating values of the top three non-trivial eigenvector coordinates (v_2, v_3, v_4) for the same ~8000 configurations shown in (b) but now colored by their values of (c) the order parameter R_g (Eq. (12)) and (d) the order parameter Ψ_6 (Eq. (15)).

of the assembly of $N = 210$ particles into quasi-2D colloidal crystals in a quadrupolar electric field. The BD simulations were matched to experiments in previous work.^{7,22–24} Fig. 2(a) shows the eigenvalue spectrum obtained from the diffusion mapping analysis. A large spectral gap after the first non-trivial eigenvalue, λ_2 , and smaller gaps after the third and fourth eigenvalues, λ_3 and λ_4 , suggest a one-dimensional nature to the data but two additional dimensions need to be considered. When plotting the data in the space of the first three eigenvectors (v_2 , v_3 , and v_4) (Figs. 2(c) and 2(d)), the data points are seen to lie on a 2D surface in the 3D space, indicating that the dynamical system is effectively two-dimensional and described primarily by the coordinates v_2 and v_3 . The v_4 values are highly correlated with the values of v_2 ; such dependencies indicate multiple eigenvectors characterizing the same dynamic pathway.³⁷

We also studied how the eigenvectors correlate with physically meaningful candidate order parameters^{7,9,15,20,21,46–48} by coloring the data in Fig. 2. Although eigenvectors from diffusion mapping can be used directly as order parameters⁴⁹ or for high-throughput screening of candidate order parameters,^{50,51} such methods are computationally expensive and were not explored in this work. Fig. 2(c) shows the data colored by values of R_g . R_g is highly correlated with v_2 , as indicated by the continuous spectrum of color vs. that coordinate. Fig. 2(d) shows the data colored by values of ψ_6 . It is found that ψ_6 is highly correlated with a combination of v_2 and v_3 . The data points plotted in (ψ_6, R_g) space in Fig. 2(b) show that the data span the regions of interest in the configuration space (based on the candidate order parameters) and are well correlated with the top non-trivial eigenvector, v_2 .

Therefore, it appears that R_g and ψ_6 are able to parameterize data embedded in the 2 significant coordinates identified by the diffusion mapping analysis. We will use these variables to build a low dimensional model of quasi-2D colloidal crystallization in electric fields.

Smoluchowski analysis of assembly trajectories

Fig. 3 shows examples of dynamic quantities obtained by analyzing a large set of ψ_6 , R_g coordinates generated from BD simulated trajectories. Results in Fig. 3 are for $N = 210$ particles with the following combinations of starting coordinates and applied non-dimensional voltages: $(\psi_6, R_g) = (0.138, 1.15)$, $V^* = 0.80$ (example of fluid condensation); $(\psi_6, R_g) = (0.3875, 1.146)$, $V^* = 0.57$ (example of grain boundary motion); and $(\psi_6, R_g) = (0.7125, 1.125)$, $V^* = 0.5$ (example of melting). Figs. 3(a) and 3(b) show the ensemble average of displacement vs. time for each starting coordinate. Positive slopes indicate the existence of driving force to increase ψ_6 (*i.e.*, ordering) or R_g (*i.e.*, expansion), whereas negative slopes indicate driving forces to decrease these quantities. The steepness of the slope characterizes the magnitude of the driving force (*i.e.*, Eqs. (17)–(19)). The slopes of each curve are qualitatively consistent with expectations for condensation ($\Delta\psi_6 \uparrow, \Delta R_g \downarrow$) and melting ($\Delta\psi_6 \downarrow, \Delta R_g \uparrow$), and the shallow slope associated with grain boundary motion shows the weak driving force for this process.

Figs. 3(c)–3(f) show the ensemble average of the four components in covariance matrix as a function of time for the same initial coordinates and applied voltage as in Figs. 3(a) and 3(b). As shown in the section titled “Theory” (Eq. (17)),

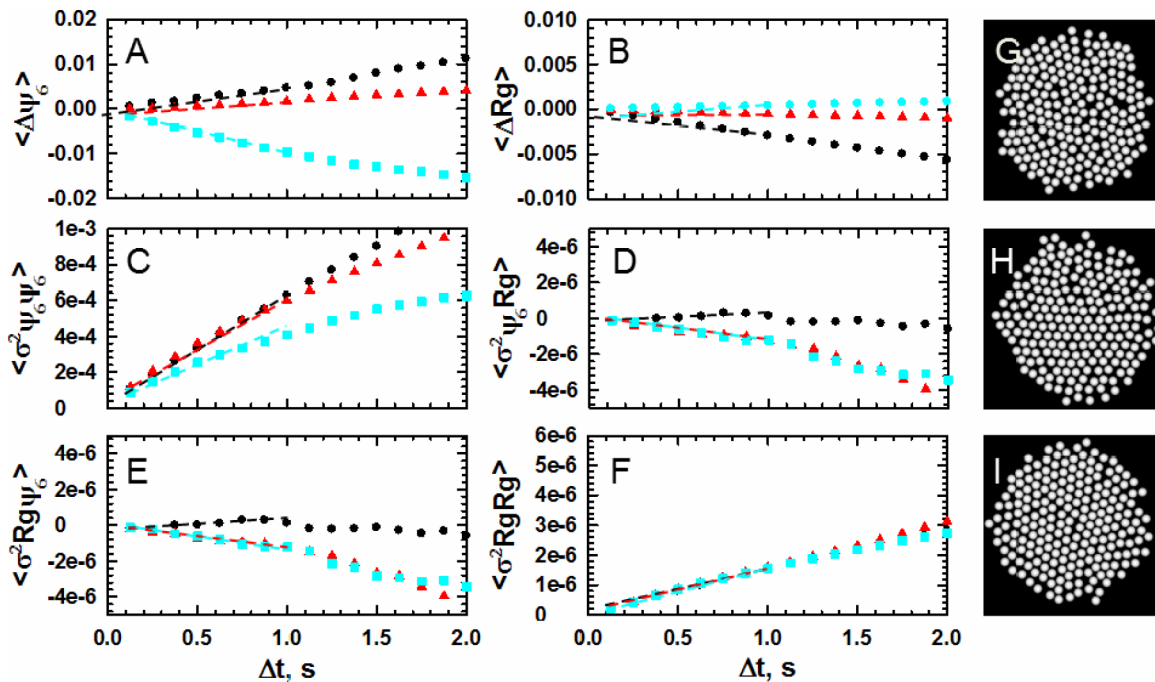


FIG. 3. Representative local order parameter trajectories used to obtain Smoluchowski equation coefficients. Results are shown for a system size of $N = 210$. Plots show ensemble average: displacement vs. time for (a) ψ_6 and (b) R_g ; displacement variance vs. time in (c) and (f); displacement covariance in (d) and (e). Representative data are shown for several different combinations of starting configurations and applied voltages including: (g) (black circles) $(\psi_6, R_g) = (0.1375, 1.146) V^* = 0.80$; (h) (red triangles) $(\psi_6, R_g) = (0.3875, 1.146) V^* = 0.57$; (i) (cyan squares) $(\psi_6, R_g) = (0.7125, 1.125) V^* = 0.50$. Linear fits to the initial slopes (illustrated by dashed lines) of the data in each plot are used in Eqs. (17)–(19) to obtain $D(x)$ and $W(x)$ in Figs. 4 and 7.

the initial slopes are proportional to the magnitude of the four components of the diffusivity tensor of the low-dimensional Smoluchowski equation (Eq. (16)). The cross terms in the diffusivities tensor reflect the coupling between both drift and diffusion along the ψ_6 and R_g coordinates. Deviations of slopes at longer times from the initial short time slopes indicate effects of drift due to the underlying landscape (that can either produce migration or localization of trajectories). Most of the fitted initial slopes via Eq. (17) have relative uncertainties (i.e., the standard value of the fitted value divided by the value itself) on the order of ~2% or smaller, which cause the resulting free energy landscape via Eq. (19) and propagation of error to have relative uncertainties of ~4%.

Field dependent landscapes (for fixed system size)

By performing the analysis illustrated in Fig. 3 at many grid points in the order parameter space, it is possible to construct coordinate dependent W and \mathbf{D} (i.e., “landscapes”) for fixed thermodynamic conditions. For the example in the present study, the voltage, V , determines the magnitude of the electric field compressing induced dipoles, and therefore acts as a global thermodynamic variable. As such, for each V^* , the relative free energy and diffusivity of each configuration can be determined to construct W and \mathbf{D} for all possible configurations. Fig. 4 shows the landscapes of W and \mathbf{D} for several values of increasing V^* for a system size of $N = 210$.

At the lowest voltage, $V^* = 0.42$ (Fig. 4(a)), the global minimum of W is located at $\psi_6, R_g \approx 0.25, 1.18$; the structure is a dense fluid consisting of several small ordered clusters (rendering I) but lacks global orientational order due to minimal coalescence in the presence of weak compression of dipoles. Fig. 4(a) shows a single example trajectory plotted on W , which illustrates compression of an expanded fluid configuration (i.e., low ψ_6 , high R_g) towards the global minimum with a relatively small free energy change (~15 kT) where it then diffuses locally.

The four diffusivity components are shown in middle column of Fig. 4(a). The $\mathbf{D}_{\psi_6\psi_6}$ component (upper left) has relatively larger values in the vicinity of $\psi_6 \approx 0.2-0.3$, which is consistent with grain boundary motion in polycrystalline structures that produces larger fluctuations in ψ_6 . $\mathbf{D}_{\psi_6\psi_6}$ decreases only slightly as R_g decreases due to hydrodynamic hindrance in compact configurations. Large regions of the diffusivity landscape cross-terms, $\mathbf{D}_{\psi_6R_g}$ and $\mathbf{D}_{R_g\psi_6}$, have values near zero, except for slightly negative values encountered in the vicinity of $\psi_6, R_g \approx (0.4, 1.18)$. These negative values in the cross-terms indicate a weak correlation between decreasing R_g and increasing ψ_6 , which is consistent with condensation being correlated with ordering. Given the different relative magnitudes of ψ_6 and R_g , the relative importance of the cross terms can also be interpreted using a correlation coefficients defined as $\rho = \mathbf{D}_{\psi_6R_g}/(\mathbf{D}_{\psi_6\psi_6}\mathbf{D}_{R_gR_g})^{0.5}$. In all cases, this correlation coefficients is less than 5%, suggesting very little correlation between R_g and ψ_6 such that the cross terms are negligible. This finding is supported by comparing BD and LDLD simulations with and without the cross terms, which are quantitatively indistinguishable.

As V^* increases to 0.5, the global minimum in W (Fig. 4(b)) shifts to $\psi_6, R_g \approx (0.6, 1.14)$, indicating both increased condensation and global ordering compared to $V^* = 0.42$. The equilibrium structure (rendering III) is characterized has a single central hexagonal close packed core with small number of peripheral fluid-like particles. While the free energy gradient in the R_g coordinate increases when increasing V^* from 0.42 to 0.5, the free energy gradient in the ψ_6 direction is shallow. For example, bi-domain crystals formed in the vicinity of $R_g \approx 1.14-1.16, \psi_6 \approx 0-0.3$ (i.e., low ψ_6 , low R_g) (rendering II) have misorientation angles close to 30°, which are metastable structures with minimal driving force for grain boundary migration. As for the diffusivity landscape at $V^* = 0.5$, $\mathbf{D}_{\psi_6\psi_6}$ and $\mathbf{D}_{R_gR_g}$ decrease as R_g become smaller, which is due to the increased hindrance at denser configuration slows down the particle arrangement behavior. At $V^* = 0.57$ (Fig. 4(c)), the global minimum in W now shifts to $\psi_6, R_g \approx (0.6, 1.14)$, with more ordered and condensed equilibrium structure (rendering VI). The diffusivity landscape components share similar features with the other voltages. At this voltage, the free energy plateau region on W (with a minimal free energy gradient) shifts and stretches to coordinates in the range around $R_g \approx 1.12-1.13, \psi_6 \approx 0-0.5$.

Field dependent assembly pathways

On the landscapes in Fig. 4(c), there are two typical assembly kinetic pathways, as exemplified by the trajectories T1 and T2 plotted on W . The T1 trajectory corresponds to rapid condensation along a steep free energy gradient where two locally ordered domains coalesce into a bi-crystal with a near maximum 30° misorientation angle. From V to VI, the bi-crystal relaxes into a single domain as one grain grows at the expense of the other.

In contrast to T1, the T2 trajectory develops higher global order via initial stochastic motion before it moves down the free energy gradient and is rapidly funneled towards the global free energy minimum. The intermediate microstructure (rendering IV) is typically characterized by domains with similar orientation (i.e., small misorientation angle). Domains with small misorientation angles easily relax during coalescence and condensation, which is consistent with a smaller free energy barrier to grain boundary motion. As a result, T2 is able to bypass the free energy plateau at low R_g to avoid the slow diffusion process encountered in the T1 trajectory, which results in much faster equilibration in the global free energy minimum single crystal. For all voltages, all diffusivity components uniformly decreases with decreasing R_g , so that paths T1 and T2 do not experience significantly different levels of friction as part of determining the total time to produce single perfect crystals.

Assembly pathway times

The low dimensional models based on the landscapes shown in Fig. 4 not only provide qualitative information about the assembly process but also quantitatively capture assembly dynamics. By evaluating statistical properties of trajectories from the full N -dimensional BD simulations

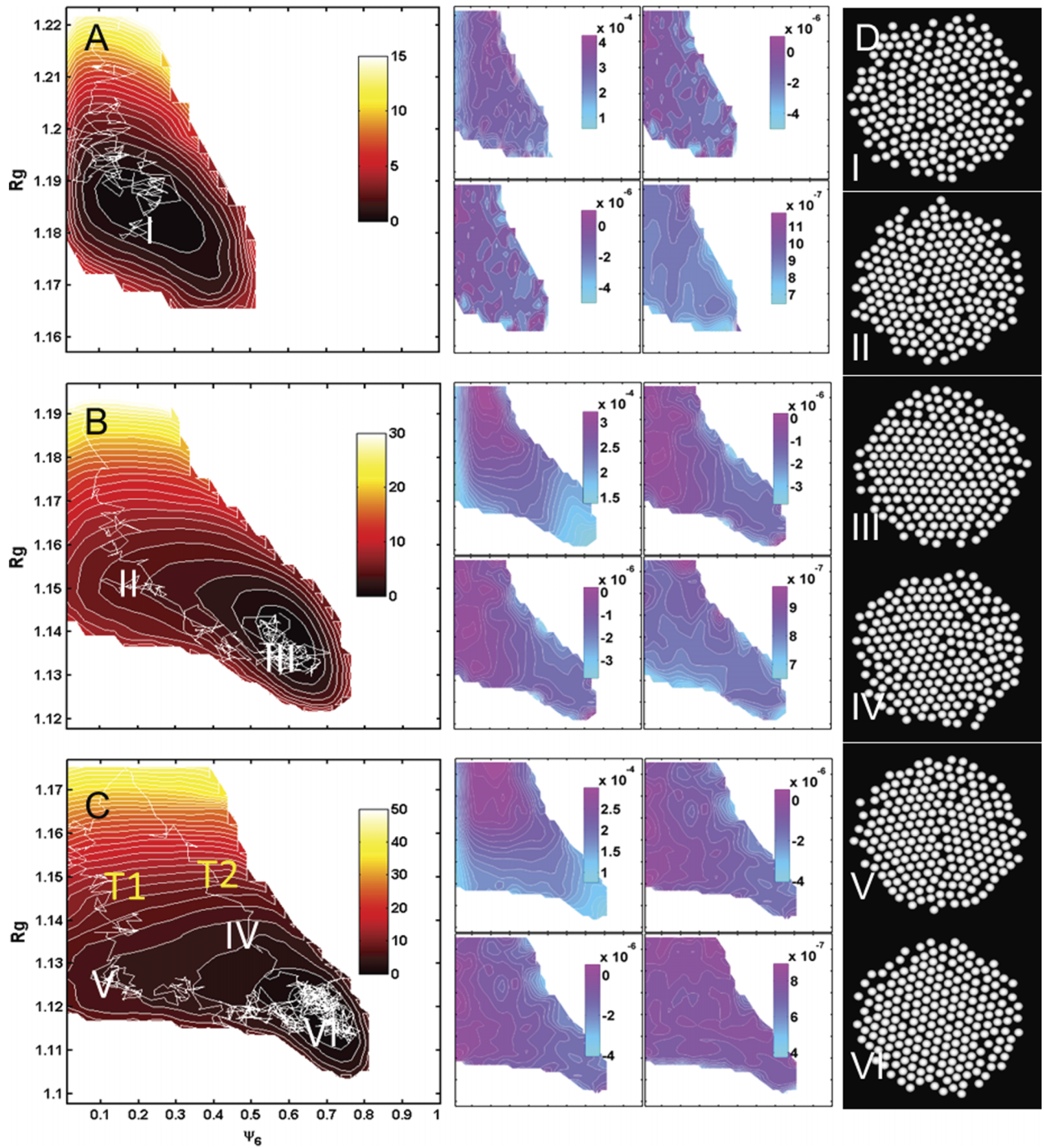


FIG. 4. Free energy and diffusivity landscapes obtained by fitting trajectories to Smoluchowski equation to BD trajectories for $N = 210$ and applied voltages of (top-to-bottom): (a) $V^* = 0.42$, (b) $V^* = 0.50$, (c) $V^* = 0.57$. Plots show (left) free energy landscapes, $W(\psi_6, R_g)/kT$ (Eq. (19)), with trajectories, marked coordinates of interest, and inset scale bars, and (middle) four components of diffusivity tensor, $\mathbf{D}/(kT \cdot s)$ (Eq. (17)), with inset scale bar and same axes as W plots (left-to-right, top-to-bottom): $\mathbf{D}_{\psi_6 \psi_6}$, $\mathbf{D}_{\psi_6 R_g}$, $\mathbf{D}_{R_g \psi_6}$, and $\mathbf{D}_{R_g R_g}$. T1 and T2 in the left most column of part (c) denote two representative trajectories following different pathways. (d) Renderings in column on far right show representative configurations for coordinates marked on W plots.

and low-dimensional Langevin dynamic (LDLD) simulations, such as the first passage times for transitions from one state to another state, it is possible to evaluate the accuracy of the LDLD model.^{7,20} Fig. 5 compares first passage time distributions from BD and LDLD simulations at $V^* = 0.57$ for $N = 210$. First passage time distributions show histograms of the times it takes to pass for the first time between initial states end states characterized by (ψ_6, R_g) coordinates on the W .

The first passage time is a distribution due to the stochastic nature of the assembly dynamics.

As depicted in Fig. 5(a), we simplify the presentation of first passage time distributions by comparing assembly processes characterized by either (1) condensation along the steep W gradient parallel to the R_g axis (plotted in Fig. 5(b)) or (2) grain boundary relaxation along the W plateau parallel to the ψ_6 axis (plotted in Fig. 5(c)). For

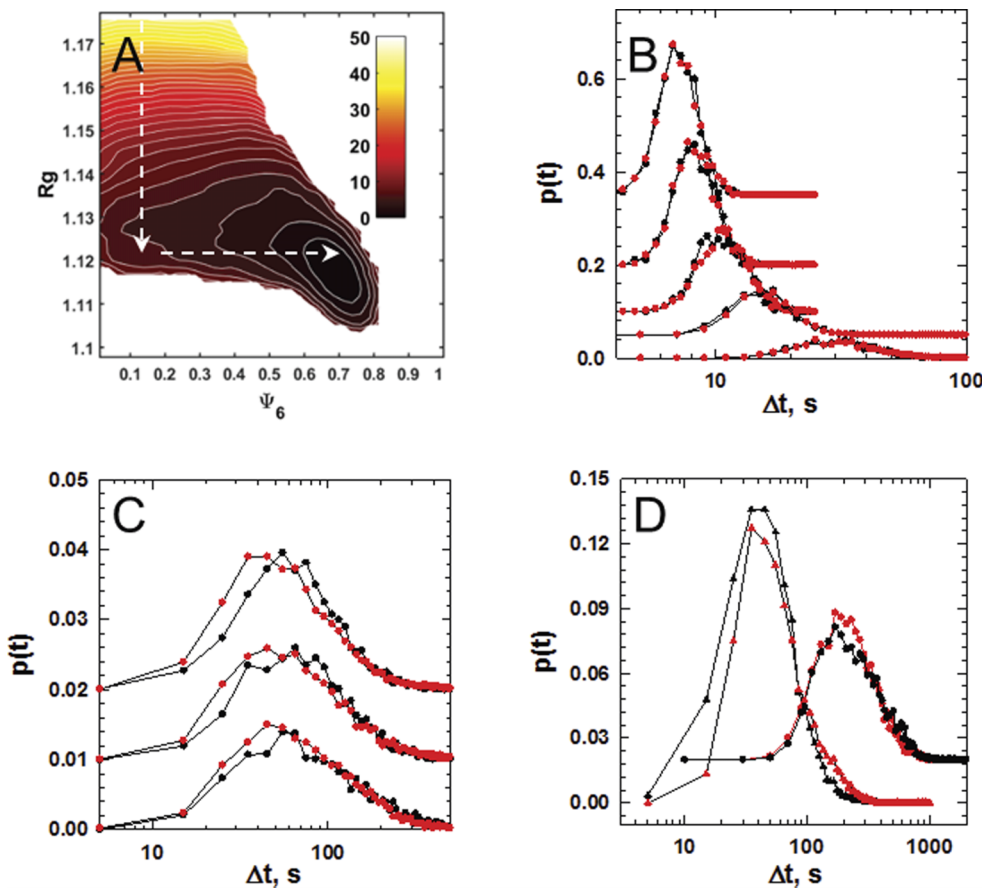


FIG. 5. First passage time distributions (FPTDs) for BD (black) and LDLD (red) trajectories during processes of condensation and grain boundary migration for system size of $N = 210$ at applied voltage of $V^* = 0.57$. (a) Schematics for the process of condensation (vertical arrow along the steep W gradient at R_g direction) and the process of grain boundary migration (horizontal arrow along the W plateau at ψ_6 direction). (b) FPTD during the condensation process measured from trajectories from starting points to end points on the R_g -axis between (top to bottom): (1.24, 1.22), (1.22, 1.20), (1.20, 1.18), (1.18, 1.16), and (1.16, 1.14). (c) FPTD during grain boundary migration process measured by tracking trajectories from starting points to end points on the ψ_6 -axis between (top to bottom): (0.4, 0.6), (0.3, 0.5), and (0.2, 0.4). (d) FPTD corresponding to T1 and T2 in Fig. 4(c) between a sink at ($\psi_6 = 0.7$ $R_g = 1.18$) (i.e., global minimum) and sources at ($\psi_6 = 0.15$ $R_g = 1.13$) (circles) and ($\psi_6 = 0.5$ $R_g = 1.14$) (triangles).

predominantly condensation processes, Fig. 5(b) shows a set of first passage time distributions for assembly trajectories between initial and final R_g coordinates specified in the figure caption. These distributions are obtained by averaging over all ψ_6 coordinates sampled during condensation. In the case of trajectories dominated by grain boundary relaxation, Fig. 5(c) shows first passage time distributions for trajectories between initial and final ψ_6 coordinates, which are averaged over all R_g coordinates. It is interesting to note the order of magnitude greater first passage time for grain boundary motion compared to condensation. Good agreement between N -dimensional BD simulations and the LDLD simulations is observed, indicating the accuracy of the W and \mathbf{D} from the Smoluchowski analysis.

Although the first passage time distributions projected onto the R_g and ψ_6 axes show the full N -dimensional BD and LDLD models agree quantitatively, they do not tell the whole story in terms of the assembly dynamics. It is still essential to use the two dimensions to characterize first passage times for different assembly pathways. For example, Fig. 5(d) shows first passage time distributions roughly corresponding to trajectories T1 and T2 in Fig. 4(c) (i.e., one starts at ($\psi_6 = 0.38$ $R_g = 1.15$) and the other one

starts at ($\psi_6 = 0.65$ $R_g = 1.16$); both terminate at the global minimum). The fast T2 trajectory makes it to the global free energy minimum single crystal nearly two orders of magnitude faster than the slow T2 trajectory that is detained on the free energy plateau corresponding to grain boundary diffusion. This large difference in first passage times is not captured by projecting the 2D trajectories either onto the ψ_6 or R_g axes as shown by the first passage times in Figs. 5(b) and 5(c).

After showing the accuracy of the LDLD model via first passage time distributions, it is possible to more completely explore the dynamic evolution of the system using the low dimensional W and \mathbf{D} in Fig. 4 to numerically solve the SE (Eq. (16)). This provides more complete information on the time evolution of states during stochastic assembly processes (e.g., compared to first passage times alone). Fig. 6 shows the solution of SE (i.e., $p(\mathbf{x}, t)$) for $N = 210$ at different voltages and observation times, Δt , with given initial conditions, $p(\mathbf{x}, 0) = \delta(\mathbf{x} - \mathbf{x}_0)$, $\mathbf{x}_0 = (0.025, 1.22)$, which corresponds to a starting fluid configuration.

At the lowest V^* , Figs. 6(a) and 6(b) show that the evolution of $p(\mathbf{x}, \Delta t)$ is characterized by slow drift and diffusion of the initial delta function towards the new equilibrium state, which is a broader distribution of

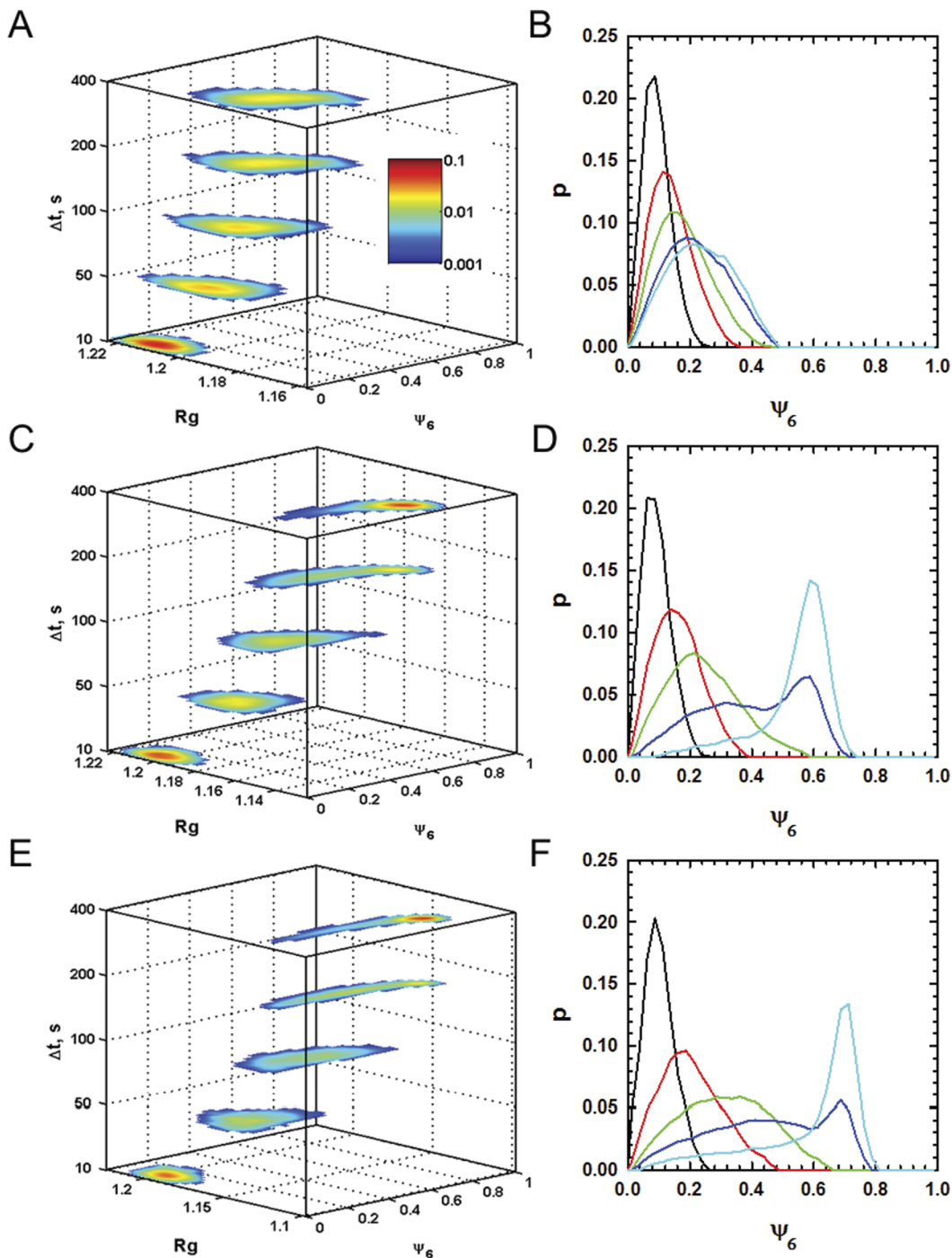


FIG. 6. Numerical solution of Smoluchowski equation to compute $p(\mathbf{x}, t)$ at observation times of $\Delta t = 10$ s, 50 s, 100 s, 200 s, and 400 s for a system size of $N = 210$ at applied voltages of: ((a) and (b)) $V^* = 0.42$, ((c) and (d)) $V^* = 0.50$, and ((e) and (f)) $V^* = 0.57$. The initial condition in all cases is $p(\mathbf{x}, 0) = \delta(\mathbf{x} - \mathbf{x}_0)$ where $\mathbf{x}_0 = (\psi_{60}, R_{g0}) = (0.025, 1.22)$. The left hand plots are two dimensional contour plots of probability density with an inset scale bar in part (a). The right hand plots are one dimensional projections of the two dimensional probability density onto the ψ_6 coordinate for: $\Delta t = 10$ s (black), 50 s (red), 100 s (green), 200 s (blue), and 400 s (cyan).

configurations centered on a more condensed fluid state. Convergence to the equilibrium Boltzmann distribution is observed to occur within ~ 200 s (most easily seen from blue and cyan curves in Fig. 6(b)). At the intermediate V^* , Figs. 6(c) and 6(d) show how $p(\mathbf{x}, \Delta t)$ more rapidly drifts towards more condensed and ordered states before a new most probable loosely packed crystal state emerges between 100 and 200 s and the equilibrium distribution is reached within ~ 400 s. At the highest V^* , which corresponds to conditions when a

single crystal is expected as the global free energy minimum configuration, Figs. 6(e) and 6(f) show how $p(\mathbf{x}, \Delta t)$ drifts even more rapidly toward evolving ordered configurations that once again reach the equilibrium distribution in ~ 400 s. The results in Fig. 6 show how the low dimensional model captures the stochastic evolution of the probability density of states at different thermodynamic conditions, which captures all dynamic information necessary to design, control, and optimize colloidal assembly schemes in this system.

System size dependent assembly pathways

Because the results in Figs. 1–6 are for a single system size of $N = 210$, we now explore different systems sizes and voltages to see how the low dimensional model and assembly behavior changes. Fig. 7 shows W and \mathbf{D} for $N = 110$, 210, and 300 at voltages that produce equilibrium structures of comparable global order and degree of condensation (*i.e.*, similar equilibrium ψ_6 and R_g ; see Fig. 7 caption for details). All W and \mathbf{D} share similar qualitative features (*e.g.*, a steep

free energy gradient followed by a plateau) and corresponding microstructures at the plateau region (*i.e.*, bicrystals at low ψ_6 and single crystals at high ψ_6) marked on the landscapes and shown in the right column of Fig. 7. Quantitative differences with increasing system size include a shift of the global minimum on each W towards somewhat higher R_g and lower ψ_6 , which is due to the smaller number of particles packing more densely and being more easily ordered. Increasing system size also produces a systematic decrease in the diagonal terms of \mathbf{D} (*i.e.*, $\mathbf{D}_{\psi_6\psi_6}$, \mathbf{D}_{RgRg}), which is most likely due to

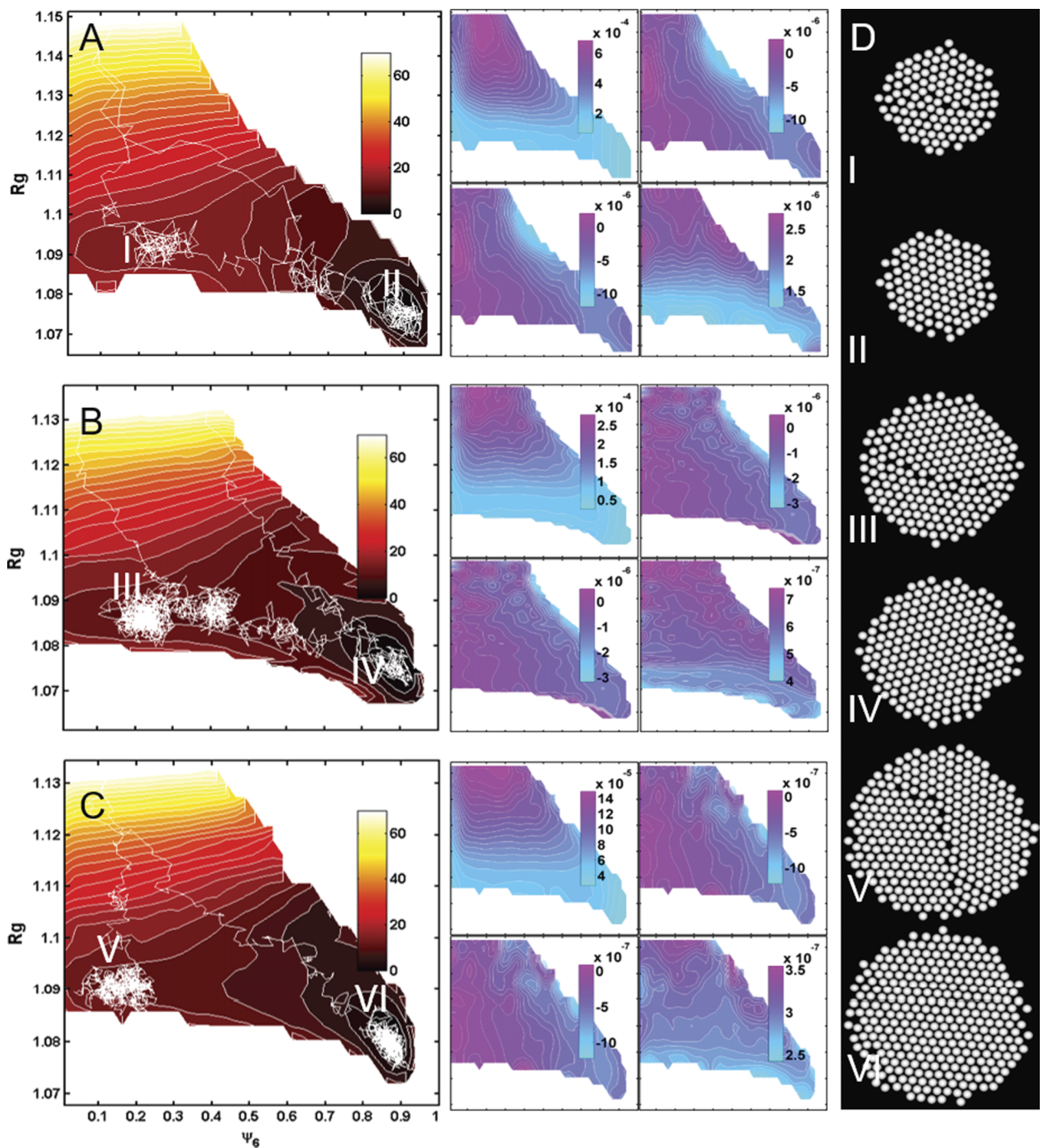


FIG. 7. Free energy and diffusivity landscapes with same formatting and procedure to obtain plots in Fig. 4 (see Fig. 4 caption), except results are now shown for different systems sizes (and applied voltages) of (top-to-bottom): (a) $N = 110$ (at $V^* = 0.85$), (b) $N = 210$ (at $V^* = 0.80$), and (c) $N = 300$ (at $V^* = 0.75$). (d) Renderings in column on far right show representative configurations for coordinates marked on W plots.

increasing hydrodynamics hindrance and associated resistance to rearrangement with increasing crowding.

Using the W and \mathbf{D} from Fig. 7, quantitative differences in the assembly kinetics can be examined by numerically solving the SEs for the three system sizes in Fig. 8 (using the same procedure and formatting as Fig. 6). Fig. 8 shows the solution of SE from initial conditions of $p(\mathbf{x}, 0) = \delta(\mathbf{x} - \mathbf{x}_0)$, $\mathbf{x}_0 = (0.025, 1.18)$ for $N = 110$, 210, and 300 for $\Delta t = 10$ s, 50 s, 100 s, 200 s, and 300 s. Within the first ~ 100 s, the distributions in all cases show rapid condensation along

the R_g direction (*i.e.*, R_g decreases) towards the W plateau near $R_g \approx 1.09$ with $p(\mathbf{x}, t)$ spanning all ψ_6 coordinates. At longer times, the probability density is depleted at the low ψ_6 region and simultaneously accumulates towards the high ψ_6 region.

The general trend in these data vs. system size is that smaller systems more rapidly approach the global free energy minimum ordered state compared to larger systems sizes. Specifically, for the $N = 110$ system at $\Delta t = 100$ s, around half of all trajectories have already reached the general vicinity

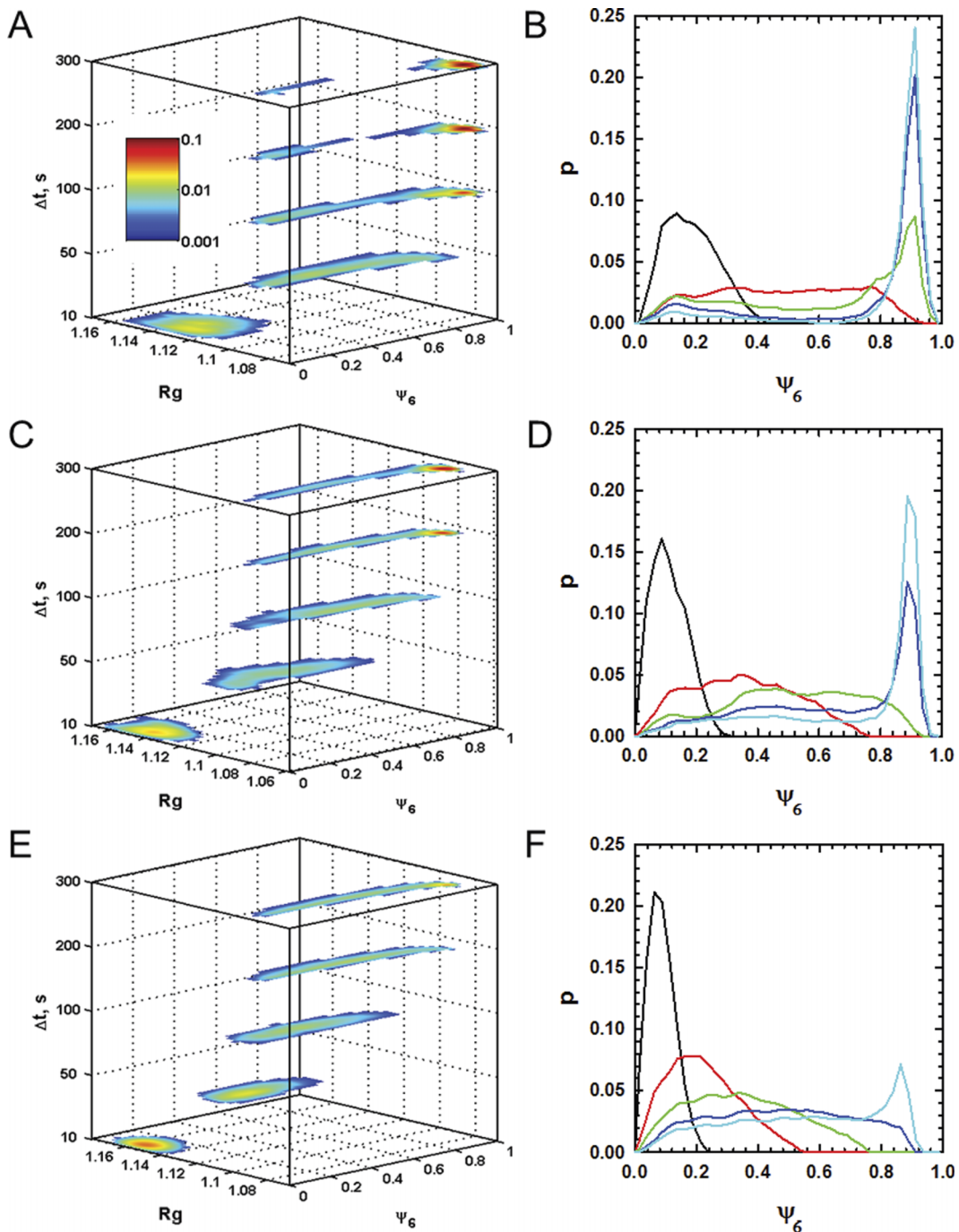


FIG. 8. Numerical solution of Smoluchowski equation to compute $p(\mathbf{x}, t)$ at observations times of $\Delta t = 10$ s, 50 s, 100 s, 200 s, and 300 s for different systems sizes (and applied voltages) of (top-to-bottom): ((a) and (b)) $N = 110$ (at $V^* = 0.85$), ((c) and (d)) $N = 210$ (at $V^* = 0.80$), and ((e) and (f)) $N = 300$ (at $V^* = 0.75$). The initial condition in all cases is $p(\mathbf{x}, 0) = \delta(\mathbf{x} - \mathbf{x}_0)$ where $\mathbf{x}_0 = (\psi_{60}, R_{g0}) = (0.025, 1.18)$. The left hand plots are two dimensional contour plots of probability density with an inset scale bar in part (a). The right hand plots are one dimensional projections of the two dimensional probability density onto the ψ_6 coordinate for $\Delta t = 10$ s (black), 50 s (red), 100 s (green), 200 s (blue), and 300 s (cyan).

of equilibrium (i.e., area under the curve at high ψ_6) whereas the rest are trapped in the plateau regions of the Ws shown in Fig. 7. From $\Delta t > 100$ s, most trajectories relax towards the equilibrium ordered state except for a small persistent portion in the vicinity of $\psi_6 \approx 0.1$. The microstructures in the region of low R_g and $\psi_6 \approx 0.1$ correspond to nearly perfect bi-crystals, which are metastable with essentially no free energy gradient to drive relaxation (which only occurs when stochastic fluctuations initiate an imbalance that causes one domain to grow at the expense of the other⁷).

With increasing system size, and particularly for the largest system here of $N = 300$, at $\Delta t = 100\text{--}200$ s, nearly all the trajectories are trapped on the W plateau, and their subsequent relaxation towards the perfect crystal state are significantly slowed compared to the $N = 110$ system. This slowing down with increasing system size can be attributed to the differences in the absolute values of the diffusivity landscapes in the region of configuration space corresponding to polycrystal relaxation towards single crystals states. Because all system sizes have plateaus on W in this region, there is little to no thermodynamic driving force all cases, so the kinetics is governed by diffusion and resistance in the ψ_6 direction. The relatively larger diffusivities in the ψ_6 coordinate for smaller systems allow trajectories to “fluctuate” more as part of relaxing towards the single crystal in the global free energy well. This system size dependent behavior has been observed in our previous experiments,²¹ which indicates the validity of the low dimensional models developed in this work. Extension of the approach here to even larger system sizes could slow dynamics to the point that assumptions underlying the analysis and interpretation in the present study (*i.e.*, ergodicity, detailed balance, thermodynamic equilibrium) could be called into question. There are no signatures of non-Markovian behavior to indicate any issues with the validity of these assumptions in the present work (all properties are independent of path and initial conditions in order parameter space).

CONCLUSIONS

We reported the development of a low-dimensional Smoluchowski equation to quantify the thermodynamics and kinetics of colloidal crystal assembly in electric fields. The dimensionality and order parameter choice was supported by a diffusion mapping analysis. Order parameters describing global order, ψ_6 , and degree of condensation, R_g , were found to yield a low-dimensional model that quantitatively captured assembly dynamics as determined by first passage times in agreement with N -dimensional dynamic data. The free energy and diffusivity landscapes from the Smoluchowski model revealed two types of kinetic pathways; one where condensation and global order emerge simultaneously to rapidly yield single domain crystals, and another one where fast condensation with local ordering, but not global ordering, results in polycrystal formation. Numerical solution of the low-dimensional Smoluchowski equation shows the temporal evolution of the probability of states for different voltages and system sizes, which quantifies

how these two variables determine the evolution of order in electric field mediated quasi-2D crystallization. Ultimately, the low dimensional model quantitatively captures slow grain boundary dynamics in the presence of vanishing free energy gradients, where friction associated with configurational rearrangements determines the relaxation rate for polycrystals to form single crystals via grain boundary motion. These low-dimensional models are currently being used to design optimal control policies for closed loop and open loop control of colloidal assembly processes designed to form single crystal structures.

ACKNOWLEDGMENTS

M.A.B. and D.M.F. acknowledge financial support by the National Science Foundation through Cyber Enabled Discovery and Innovation Grant (Nos. CMMI-1124648 and CMMI-1125188).

- ¹S. C. Glotzer and M. J. Solomon, *Nat. Mater.* **6**(7), 557–562 (2007).
- ²M. Grzelczak, J. Vermant, E. M. Furst, and L. M. Liz-Marzán, *ACS Nano* **4**(7), 3591–3605 (2010).
- ³O. D. Velev and S. Gupta, *Adv. Mater.* **21**(19), 1897–1905 (2009).
- ⁴P. F. Damasceno, M. Engel, and S. C. Glotzer, *Science* **337**(6093), 453–457 (2012).
- ⁵J. A. Millan, D. Ortiz, G. van Anders, and S. C. Glotzer, *ACS Nano* **8**(3), 2918–2928 (2014).
- ⁶P. F. Damasceno, M. Engel, and S. C. Glotzer, *ACS Nano* **6**(1), 609–614 (2011).
- ⁷T. D. Edwards, Y. Yang, D. J. Beltran-Villegas, and M. A. Bevan, *Sci. Rep.* **4**, 6132 (2014).
- ⁸J. J. Juarez and M. A. Bevan, *Adv. Funct. Mater.* **22**(18), 3833–3839 (2012).
- ⁹Y. Xue, D. J. Beltran-Villegas, X. Tang, M. A. Bevan, and M. A. Grover, *IEEE Trans. Control Syst. Technol.* **22**, 1956 (2014).
- ¹⁰M. A. Bevan, D. M. Ford, M. A. Grover, B. Shapiro, D. Maroudas, Y. Yang, R. Thyagarajan, X. Tang, and R. M. Sehgal, *J. Process Control* **27**, 64–75 (2015).
- ¹¹S. Sriraman, I. G. Kevrekidis, and G. Hummer, *J. Phys. Chem. B* **109**(14), 6479–6484 (2005).
- ¹²H. Risken and T. Frank, *The Fokker-Planck Equation: Methods of Solution and Applications* (Springer, 1996).
- ¹³D. I. Kopelevich, A. Z. Panagiotopoulos, and I. G. Kevrekidis, *J. Chem. Phys.* **122**, 044908 (2005).
- ¹⁴R. B. Best and G. Hummer, *Phys. Rev. Lett.* **96**(22), 228104 (2006).
- ¹⁵D. J. Beltran-Villegas, R. M. Sehgal, D. Maroudas, D. M. Ford, and M. A. Bevan, *J. Chem. Phys.* **135**(15), 154506 (2011).
- ¹⁶I. T. Jolliffe, *Principal Component Analysis* (Springer, 2002).
- ¹⁷A. L. Ferguson, A. Z. Panagiotopoulos, I. G. Kevrekidis, and P. G. Debenedetti, *Chem. Phys. Lett.* **509**(1–3), 1–11 (2011).
- ¹⁸R. Coifman, I. Kevrekidis, S. Lafon, M. Maggioni, and B. Nadler, *Multiscale Model. Simul.* **7**(2), 842–864 (2008).
- ¹⁹D. J. Beltran-Villegas, R. M. Sehgal, D. Maroudas, D. M. Ford, and M. A. Bevan, *J. Chem. Phys.* **132**(4), 044707 (2010).
- ²⁰D. J. Beltran-Villegas, R. M. Sehgal, D. Maroudas, D. M. Ford, and M. A. Bevan, *J. Chem. Phys.* **137**(13), 134901 (2012).
- ²¹T. D. Edwards, D. J. Beltran-Villegas, and M. A. Bevan, *Soft Matter* **9**(38), 9208–9218 (2013).
- ²²J. J. Juarez and M. A. Bevan, *J. Chem. Phys.* **131**, 134704 (2009).
- ²³J. J. Juarez, J.-Q. Cui, B. G. Liu, and M. A. Bevan, *Langmuir* **27**(15), 9211–9218 (2011).
- ²⁴J. J. Juarez, B. G. Liu, J.-Q. Cui, and M. A. Bevan, *Langmuir* **27**(15), 9219–9226 (2011).
- ²⁵S. K. Smoukov, S. Gangwal, M. Marquez, and O. D. Velev, *Soft Matter* **5**(6), 1285–1292 (2009).
- ²⁶N. I. Zheludev and Y. S. Kivshar, *Nature Mater.* **11**(11), 917–924 (2012).
- ²⁷P. Bahukudumbi, W. N. Everett, A. Beskok, G. H. Huff, D. Lagoudas, Z. Ounaires, and M. A. Bevan, *Appl. Phys. Lett.* **90**, 224102 (2007).
- ²⁸J. J. Juarez, P. P. Mathai, J. A. Liddle, and M. A. Bevan, *Lab Chip* **12**(20), 4063–4070 (2012).
- ²⁹J. J. Juarez, S. E. Feicht, and M. A. Bevan, *Soft Matter* **8**(1), 94–103 (2012).

- ³⁰G. M. Bell, S. Levine, and L. N. McCartney, *J. Colloid Interface Sci.* **33**(3), 335–359 (1970).
- ³¹S. Anekal and M. A. Bevan, *J. Chem. Phys.* **125**, 034906 (2006).
- ³²D. L. Ermak and J. A. McCammon, *J. Chem. Phys.* **69**(4), 1352–1360 (1978).
- ³³J. F. Brady and G. Bossis, *Annu. Rev. Fluid Mech.* **20**, 111–157 (1988).
- ³⁴D. J. Jeffrey and Y. Onishi, *J. Fluid Mech.* **139**, 261–290 (1984).
- ³⁵J. W. Swan and J. F. Brady, *Phys. Fluids* **19**(11), 113306 (2007).
- ³⁶R. R. Coifman, Y. Shkolnisky, F. J. Sigworth, and A. Singer, *IEEE Trans. Image Process.* **17**(10), 1891–1899 (2008).
- ³⁷A. L. Ferguson, A. Z. Panagiotopoulos, P. G. Debenedetti, and I. G. Kevrekidis, *Proc. Natl. Acad. Sci. U. S. A.* **107**(31), 13597–13602 (2010).
- ³⁸B. I. Halperin and D. R. Nelson, *Phys. Rev. Lett.* **41**(2), 121–124 (1978).
- ³⁹A. W. C. Lau and T. C. Lubensky, *Phys. Rev. E* **76**(1), 011123 (2007).
- ⁴⁰C. W. Gardiner, *Handbook of Stochastic Methods for Physics, Chemistry, and the Natural Sciences*, 2nd ed. (Springer, Berlin, 2009).
- ⁴¹J. A. Trangenstein, *Numerical Solution of Hyperbolic Partial Differential Equations* (Cambridge University Press, 2009).
- ⁴²J. Baumgartl and C. Bechinger, *Europhys. Lett.* **71**, 487–493 (2005).
- ⁴³T. O. Pangburn and M. A. Bevan, *J. Chem. Phys.* **123**, 174904 (2005).
- ⁴⁴D. J. Beltran-Villegas, T. D. Edwards, and M. A. Bevan, *Langmuir* **29**(40), 12337–12341 (2013).
- ⁴⁵R. A. Mansbach and A. L. Ferguson, *J. Chem. Phys.* **142**(10), 105101 (2015).
- ⁴⁶D. J. Beltran-Villegas and M. A. Bevan, *Soft Matter* **7**(7), 3280–3285 (2011).
- ⁴⁷G. E. Fernandes, D. J. Beltran-Villegas, and M. A. Bevan, *J. Chem. Phys.* **131**, 134705 (2009).
- ⁴⁸G. E. Fernandes, D. J. Beltran-Villegas, and M. A. Bevan, *Langmuir* **24**, 10776–10785 (2008).
- ⁴⁹C. R. Laing, T. A. Frewen, and I. G. Kevrekidis, *Nonlinearity* **20**(9), 2127 (2007).
- ⁵⁰B. Peters and B. L. Trout, *J. Chem. Phys.* **125**(5), 054108 (2006).
- ⁵¹A. Ma and A. R. Dinner, *J. Phys. Chem. B* **109**(14), 6769–6779 (2005).